

Measurements of Absolute Cross Sections for Electron-Impact Ionization of Doubly Charged Rare Gas Ions: Ne^{2+} , Ar^{2+} , Kr^{2+} , and Xe^{2+}

Atsushi MATSUMOTO,* Atsunori DANJO,** Shunsuke OHTANI,
Hirosi SUZUKI,*** Hiroyuki TAWARA, Toshinobu TAKAYANAGI,***
Kazuyoshi WAKIYA,*** Ichihiro YAMADA, Masuhiro YOSHINO****
and Takato HIRAYAMA*****

National Institute for Fusion Science,[#] Nagoya 464-01

(Received October 24, 1989)

The technique of crossed electron-ion beams has been employed to measure the absolute cross sections for single ionization of Ne^{2+} , Ar^{2+} , Kr^{2+} and Xe^{2+} ions at electron energies ranging from below threshold to 1000 eV. Detailed descriptions of the experimental apparatus and procedures to determine the absolute cross sections are presented, and are discussed check points for reliability and consistency as well as possible contributions of metastable contents in the ion beam. The total systematic error in the cross sections is estimated to be within $\pm 9\%$. A distinct discrepancy is observed for Ne^{2+} between the measured cross section curve and results of semiempirical calculation using the Lotz formula. The cross sections for Ar^{2+} , Kr^{2+} and Xe^{2+} reveal significant contributions from excitation-autoionization processes in addition to direct ionization, especially in the near threshold energy regions.

§1. Introduction

Besides a continuing intrinsic interest, the electron impact ionization of ions is of particular importance in understanding or modeling of both laboratory and astrophysical plasmas. In 1961, Dolder and his colleagues¹⁾ obtained the accurate electron impact ionization cross sections for He^+ using a crossed electron and ion beams technique, and demonstrated that the technique could provide the most accurate and detailed information. Since then electron impact ionization cross sections for ions have been measured for a number of ion species and data have been

compiled.^{2,3)}

Cross section data for multiply charged ions were, however, rather scarce because of difficulties of obtaining sufficient ion beam intensity, until powerful multiply charged ion sources such as electron cyclotron type have been developed intensively in recent years. Several systematic investigations are recently being made for multiply charged ions using the crossed beams technique mainly by two research groups at Oak Ridge National Laboratory (in collaboration with JILA)⁴⁾ and at University of Giessen.⁵⁾

Various theoretical (classical, semiclassical and quantum) approaches have been developed so far but the agreement with experiments is not always satisfactory, which is mainly caused by the inherent difficulties of a three (or many) body problem and by the fact that, in addition to the direct ionization, indirect ionization processes of complex mechanisms, for instance the excitation-autoionization or resonant recombination-double-autoionization, often contribute to the ionization process.⁶⁾

In the present paper, systematic data for

* Permanent address: Hiroshima Institute of Technology, Saeki-ku, Hiroshima 731-51.

** Permanent address: Department of Physics, Niigata University, Niigata 950-21.

*** Permanent address: Department of Physics, Sophia University, Chiyoda-ku, Tokyo 102.

**** Permanent address: Laboratory of Physics, Shibaura Institute of Technology, Omiya 330.

***** Permanent address: Department of Physics, Gakushuin University, Toshima-ku, Tokyo 171.

[#] Formerly Institute of Plasma Physics, Nagoya University.

single ionization cross sections of doubly charged rare-gas ions, which have the ns^2np^4 electron configurations in the outershells, are reported. The crossed electron and ion beams technique is used in the present measurement, where doubly charged rare-gas ions are extracted from an electron cyclotron resonance (ECR) ion source. By studying ions of the same charge from the same group of the periodic table, systematic effects may be revealed which depend mainly on the inner shell electron structure. It is the main purpose of this paper to present detailed experimental description and several consistency checks as well as to summarize the data which were briefly reported previously.⁷

§2. Experimental

2.1 General

The present experiments are made with the crossed beams of electrons and ions, similar to those developed by Dolder and Peart.⁸ Figure 1 shows a schematic drawing of the present apparatus. Ions are produced from the corresponding rare gases in the ECR ion source, continuously extracted and accelerated by 3.0 kV to produce a 6.0 keV beam (except for

Xe^{2+} where 2.84 kV was supplied). The doubly charged ion beam is passed through an exit slit of a mass-selector and enters an interaction chamber, which is evacuated with a 450 l/s turbomolecular pump and a cryogenic pump down to the operating pressure lower than 1×10^{-7} Pa. After passing through an electrostatic quadrupole lens (doublet) and a pair of defining slits, the ion beam intersects an electron beam at right angles. A movable L-shaped shutter with a fine slit is used to measure current densities of both the electron and ion beams at the interaction region. By a 45° parallel plate electrostatic analyzer, the product triply charged ions are spatially separated from the parent ions.

Ionization cross sections are derived from the measured quantities by the expression⁸

$$\sigma(E) = \frac{qe^2 v_e v_i}{(v_e^2 + v_i^2)^{1/2}} \frac{FR}{IJD}, \quad (1)$$

where $\sigma(E)$ is the absolute cross section at the electron energy E , R is the signal count rate, I , J and v_i , v_e are the currents and velocities of ions and electrons, respectively, q is the charge of the incident ion in units of electron charge e , and D is the efficiency of detector with

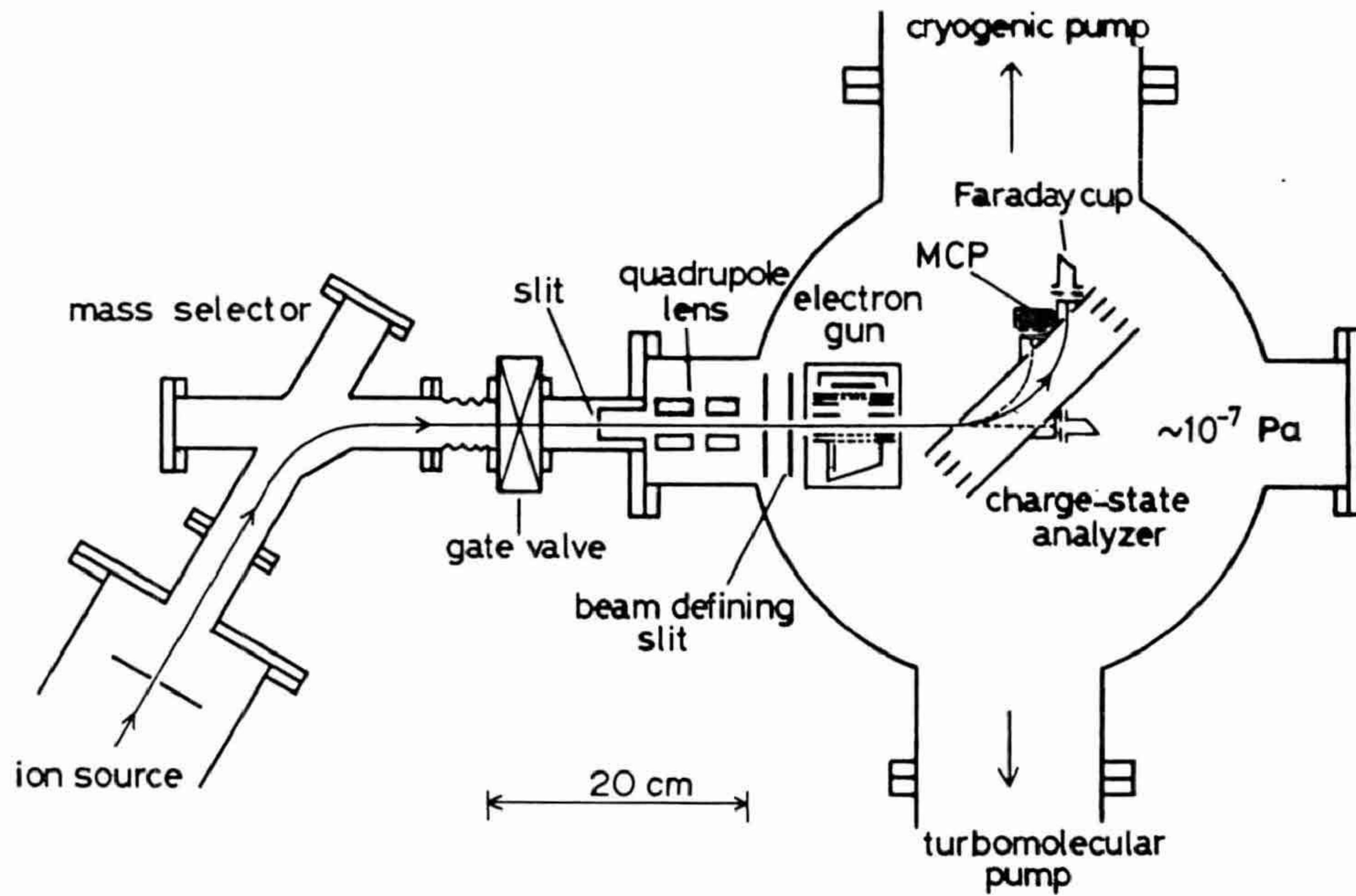


Fig. 1. Schematic diagram of the apparatus for the crossed electron-ion beam experiments to measure the ionization cross section of atomic ions.

which the product ions are collected and detected. The form factor F , which takes account of the spatial overlap of the two beams, is given by

$$F = \frac{\int i(z) dz \int j(z) dz}{\int i(z) j(z) dz}, \quad (2)$$

where $i(z)$ and $j(z)$ are the relative distributions of the ion and electron current densities along the z axis, which is perpendicular to the axes of the two beams.

In the following subsections, the experimental procedures and consistency checks are described in detail and several sources of errors and difficulties are discussed.

2.2 Ion beam

One of the most elaborate steps of the procedures in this experiment is to obtain a well-tuned ion beam. The present ion beam is obtained from the ECR ion source (called TPM-I in the IPP/Nagoya), which had been described previously.⁹ Before every experimental run, the ion beam is carefully optimized to obtain a sufficient beam intensity, a minimum background noise and a complete transmission of the beams from the intersection region to the proper detectors. An optimum condition of the ion beam is determined by scanning potentials applied to lenses and deflectors in both the beam extraction chamber and interaction chamber as well as by controlling the ion source condition.

The ion beam is collimated with two beam-defining apertures. The size of the ion beam is determined mainly by the second aperture ($1 \times 1 \text{ mm}^2$) placed just in front of the interaction region. To minimize the background noise which originates from ion scattering at the aperture edges, the apertures are knife-edged. Although the ion beam just after the aperture is regarded as nearly parallel, it is subject to diverge to some extent due to the space charge of its own. To ensure complete transmission, the entrance and exit slits of the charge state analyzer are made sufficiently large ($6 \times 18 \text{ mm}^2$) compared to the ion beam size. A transmission check is done by scanning the potential applied to the analyzer; the focal

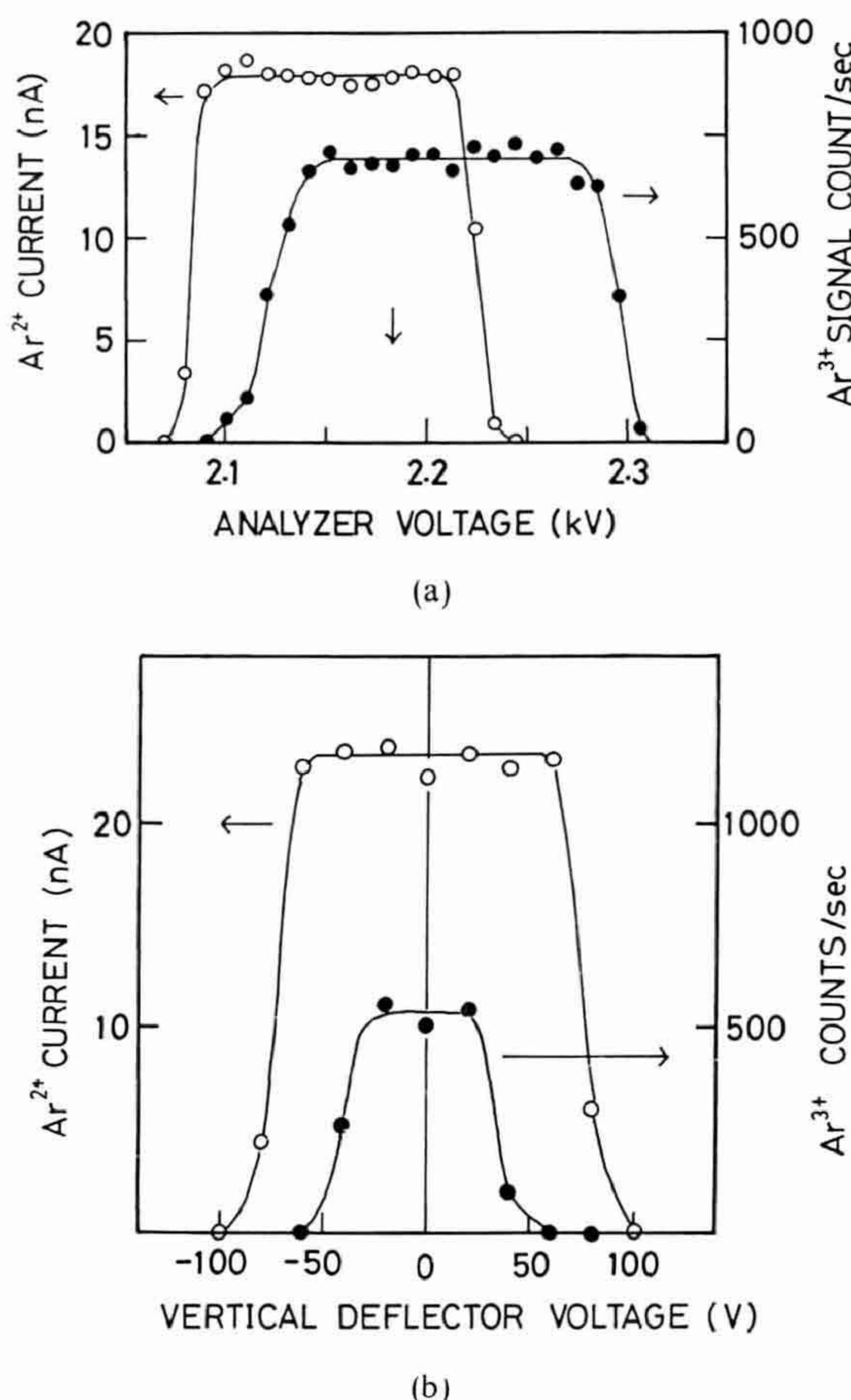


Fig. 2. (a) Current of primary ion beam and counts of product ions versus potential applied to the charge state analyzer. (b) Current of primary ion beam and counts of product ions versus voltage of the vertical deflector just behind the interaction region. Each point was accumulated for 10 s at the electron energy of 100 eV.

point of the analyzer moves horizontally along the grounded exit plate according to the applied voltage. If the beam is transmitted completely, the signals from the respective detectors should show flat-topped distribution as a function of the analyzer voltage. Figure 2(a) shows an example of this transmission check. Every data point is taken in 10 s at a fixed electron energy (usually 100 eV). The difference of the center position of each flat top between the primary and the product ion beams is presumably due to geometrical misalignment and/or an aberration of the analyzer. The applied voltage to the analyzer is then fixed at the center position of the flat-topped region where

the parent and product ion beams are overlapped, as indicated by an arrow in Fig. 2(a). An additional check of the beam transmission is made by vertical beam scanning with a deflector just behind the interaction region. Figure 2(b) shows an example of this vertical transmission check, also indicating good flat-topped distributions of both beams. The applied potential to the deflector is fixed normally at zero to several volts during the measurements.

The parent ion beam is collected in a Faraday cup with a repeller electrode at its entrance, which suppresses escaping of secondary electrons produced inside the cup. In order to check complete collection, apparent cross section are measured as a function of the potential of the repeller electrode. No systematic change is found in the measured cross sections with variation of potential in the range from +100 to -300 V. Usually -90 V is applied to the repeller electrode during the measurements.

A microchannel plate (MCP) is used for the detection of the product ions, because it has a large sensitive area with nearly uniform sensitivity. The MCP used in the present experiment (Hamamatsu F1551-21) is of a tandem type with an effective aperture of 14 mm in diameter. Two grid electrodes made of fine tungsten wires (30 μm in diameter) having approximately 100% ion transmission are placed in front of the entrance surface of the MCP: the first is grounded and the potential of the second can be varied. This assembly is mounted on the grounded analyzer plate and is contained in a grounded box. The potential applied to the entrance surface of the MCP is -2.0 kV. Therefore, the total energy of product ions impinging on the MCP is 12 keV (except for Xe^{3+}). Secondary electrons emitted from the MCP can be repelled by the second grid whose potential is usually 400 V negative to the MCP surface. Charge pulses from the MCP are processed and counted using a conventional arrangement of amplifier, discriminator and scalers. The output pulses from the MCP contain not only signals due to product ions but also those due to dark current and background noises. Although signals are not clearly separated from background noises in the pulse height distributions, the

discrimination level is determined as follows. The apparent cross sections are measured as a function of the discrimination level. They are found to be constant up to critical levels, above which they decrease with increasing discrimination level.

2.3 Electron beam

The electron source assembly consists of an indirectly-heated oxide cathode, a reflector plate, four electrodes, a collision box and a Faraday cup. All are made of stainless steel except for the cathode. The assembly is surrounded by a grounded box made of μ -metal, which shields stray magnetic field originating from the ion source. The cathode is taken from an electron tube (Toshiba 6AS7G) with a rectangular ($4 \times 28 \text{ mm}^2$) shape and mounted parallel to the ion beam axis. At the rear side of the cathode is placed the reflector plate, to which the potential of about 10 V negative to the cathode is applied. The electron beam is extracted from the cathode and accelerated by a set of slotted electrodes: the slots are rectangular ($5 \times 18 \text{ mm}^2$) and the two slots subsequent to the cathode are covered with mesh so that uniform electric fields are formed between the two electrodes and between the cathode and the first electrode. The first electrode is used to chop the electron beam. The remaining electrodes are usually grounded. The beam is collimated by an entrance slit ($3 \times 18 \text{ mm}^2$) of the collision box, which has also apertures for an ion beam passage and an open base for passage of a vertically scanning shutter. After intersecting the ion beam, the electron beam is collected in the Faraday cup and its averaged current is measured with an electrometer (Keithley 610C).

The chopping of the electron beam is made by applying a pulsed voltage of about a half of the cathode voltage V_e for low electron energy $V_e \leq 200 \text{ V}$ to the first electrode which is kept to -15 V against the cathode. This provides a roughly uniform field between the cathode and the second grounded electrode. For higher electron energies, $V_e > 200 \text{ V}$, on the other hand, pulses of constant amplitude of 115 V is applied to the first electrode. These operations give rather flat spatial distribution of the electron beam in the present case (see Fig. 5).

The duty factor of the chopped electron beam differs from that of the reference pulse generator (50% duty), owing to the delay in the pulse amplifier circuit. The duty factor, measured directly by observing the current of the Faraday cup on an oscilloscope, is found to be between 47.0 and 49.4%, depending slightly on the output amplitude.

The Faraday cup has an inclined bottom and an insulated plate inside supplied by a certain potential so as to prevent secondary electrons from escaping. Fine tungsten wires of $30\text{ }\mu\text{m}$ diameter are stretched at every 3 mm distance both vertically and horizontally at the entrance of Faraday cup and at the exit of the collision box. These meshes allow the beam to transmit nearly 100% and prevent the penetration of any electric field into the interaction region.

Systematic errors due to both escaping secondary electrons and stray electrons are examined by observing the beam currents as a function of the potential V_c and V_r , respectively, where V_c is the potential applied to the plate inside the Faraday cup and V_r is the biased potential of the Faraday cup. The errors are estimated to be less than 0.5% for escaping electrons and less than 3.0% for stray electrons at all electron energies studied under the condition of $V_c=50\text{ V}$ and $V_r=0\text{ V}$, where the cross sections are measured.

The actual electron beam energy in the collision volume generally differs from the potential applied to the cathode due to the effects of beam space charge, surface contact potential and thermal energy from the cathode. These effects cause both energy shift and spread of the electron beam, which are serious in particular at low impact energies.

In order to check the space charge effect, which depends on the electron current, apparent ionization cross sections at some electron energies were measured for Ar^{2+} ions as a function of the electron current, and the results are shown in Fig. 3. Apparent cross sections remain constant in low current region but decrease as the current increases. The present cross section measurements were made in the lowest current region where the apparent cross sections show no variation with the electron current. The energy shift and spread were

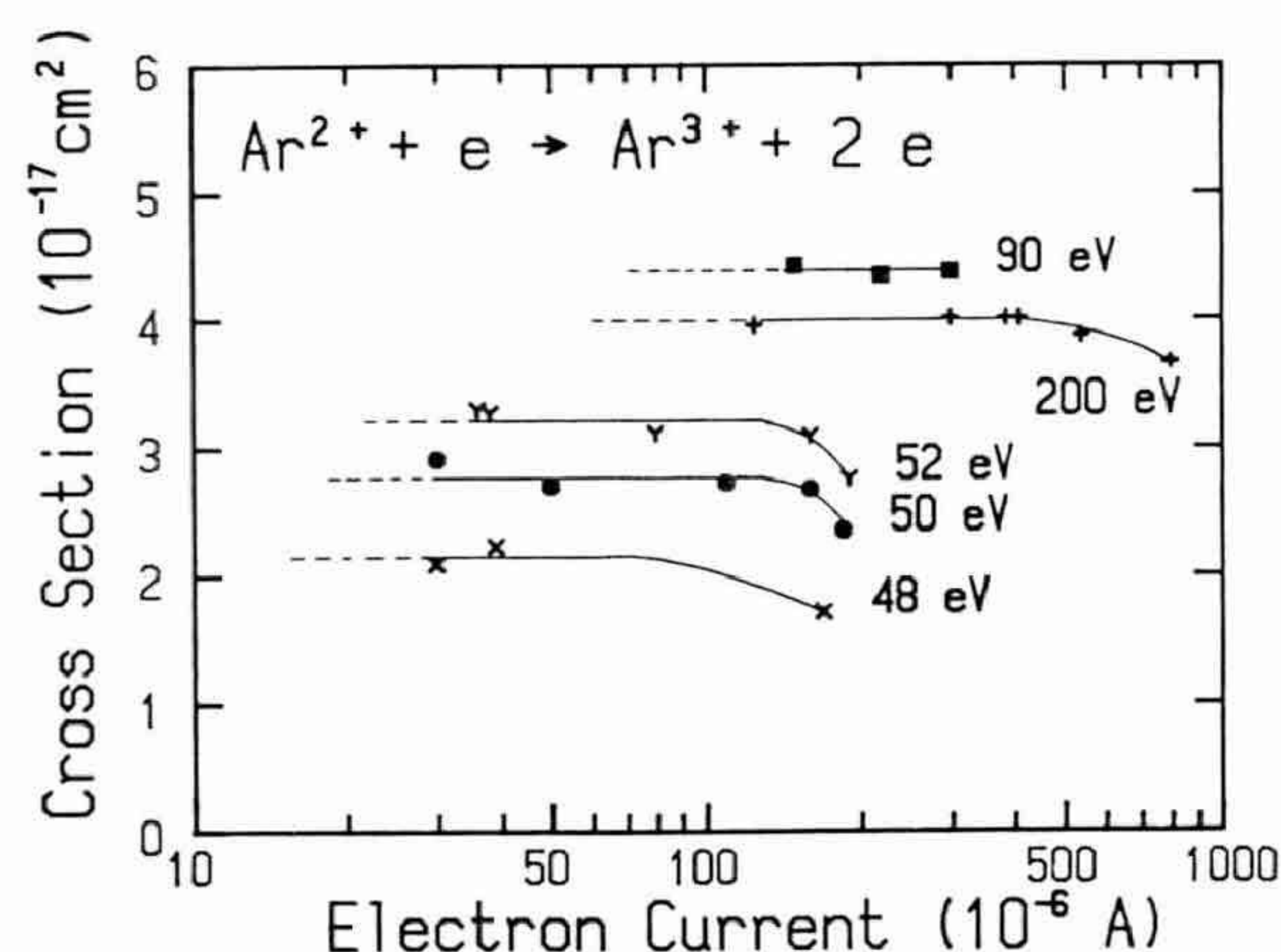


Fig. 3. Apparent ionization cross sections for several electron energies as a function of the electron current.

roughly estimated to be within 1 eV from the cross section behavior around the thresholds. Thus, the electron energy was assumed to be determined from the cathode potential and no corrections were made for the energy shift.

2.4 Beam modulation and data acquisition

In the crossed beams experiment the signal is usually very minute due to a tenuous beam intensity of ions and must be separated from backgrounds of the same particles formed by extraneous processes. The double beam modulation technique, which was developed by Harrison and his colleagues,¹⁰⁾ is used in the present experiment.

The ion and electron beams are modulated according to the time sequence shown in Fig. 4, and pulses due to the signals and backgrounds are fed into two scalers which are gated by the pulse trains shown in the figure. The ion beam is pulsed on and off with a frequency of usually 500 Hz and with a duty factor of 50%. The electron beam is similarly pulsed but phased off half a way through the ion beam. Thus the true signal is obtained by subtracting the counts registered on scaler 1 from those on 2. Systematic errors will, however, arise if the ion and/or electron currents are not constant for the duration of each pulse. In order to compensate these sources of error the pulses of ion and electron beam can be interchanged automatically at every 500 ion pulse (A+B mode). Apparent cross section data are sampled in both modes (A mode and

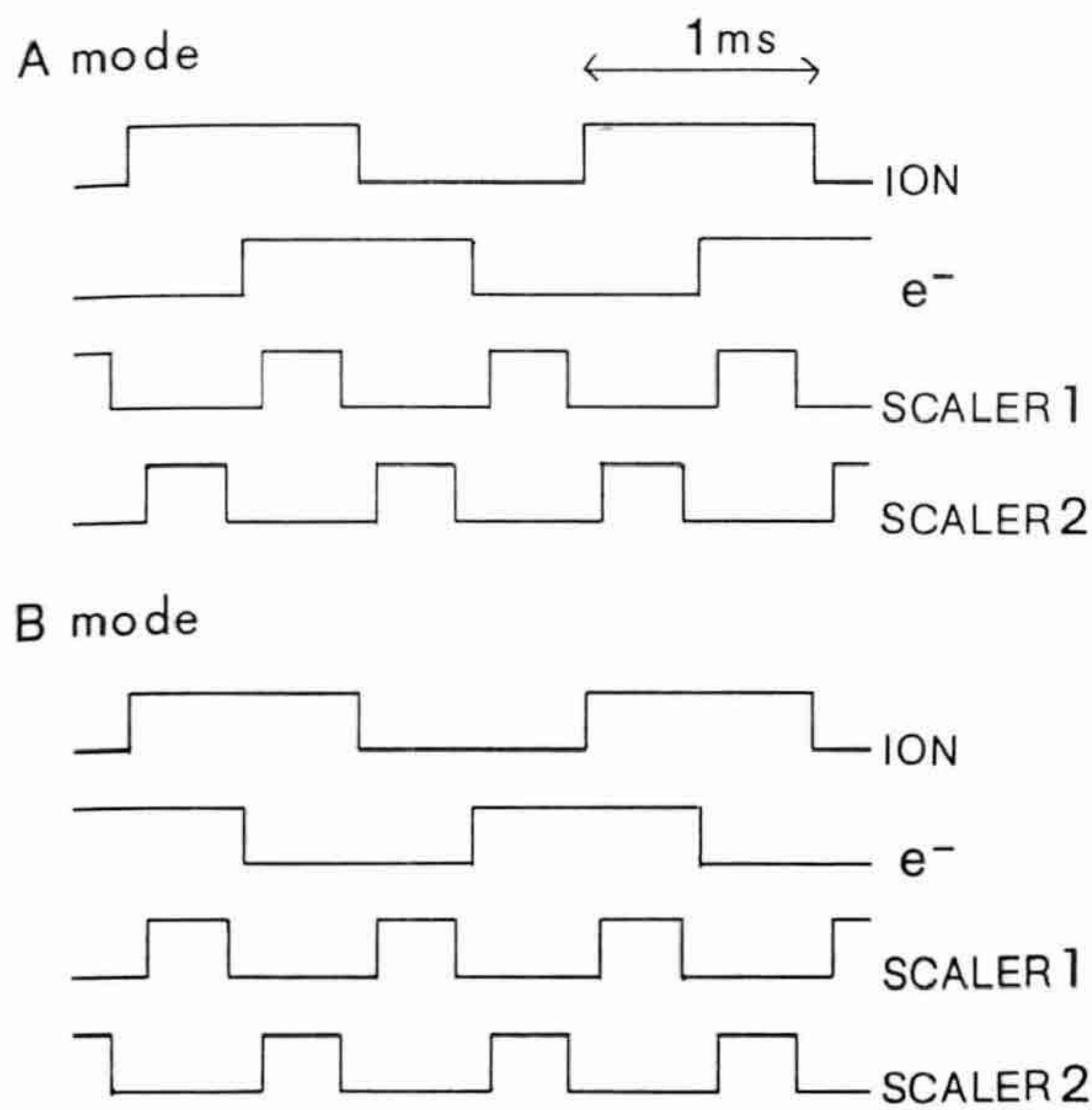


Fig. 4. Schematic diagram of the beam modulation sequence.

A+B mode), but no difference between the two modes is observed within statistical error. Usually data are acquired in A+B mode in the present experiment.

The ion beam is chopped by a deflector in the ion extraction chamber of the ion source, while the electron beam is chopped by the grid electrode to which the pulsed potential with -15 V D.C. offset is applied as described in subsection 2.3. Both the ion and electron currents are derived from the averaged currents \bar{I} , \bar{J} measured by the respective Faraday cups and the respective duty factor; i.e.,

$$I = \bar{I}/D_i, \quad (3)$$

and

$$J = \bar{J}/D_e. \quad (4)$$

The duty factor of the ion beam is exactly 50% but that of the electron beam is slightly lower

than 50%, as described previously. In addition, the electron beam had definite rise and fall times (less than 10 μ s). Then, the timing and duration of the gate pulse was carefully determined. The typical duty factor of the gate was about 17% (see Table I).

Cross sections were measured by accumulating counts of the scalers 1 and 2 in a certain period of time (usually 300 s) at every electron energy. To compensate for the fluctuation of the ion beam current, which depends on the ion source condition, the current was integrated during that period by connecting a voltage-to-frequency converter followed by a scaler to an electrometer output. From factors were measured just before or just after this period.

A considerable part of the background noises was due to the ion beam. Stray electrons could not impinge onto the MCP because of its high negative potential (-2.0 kV) at the entrance surface. Table I shows examples of raw data for Ne^{2+} , Ar^{2+} , Kr^{2+} and Xe^{2+} at the electron energy of 100 eV.

One of the most important tests in crossed-beam experiments is to determine whether the cross sections are zero below its threshold energy. However, the cross sections obtained in the present experiments were not zero even below thresholds except for Ne^{2+} . Two reasons are considered to be responsible for nonzero cross sections below thresholds: one is the pressure-modulated backgrounds which could not be avoided even by the beam chopping techniques. The other is the presence of long-lived metastable ions in the parent ion beam used. In order to check the pressure modulation, apparent cross sections were obtained at three chopping frequencies 250, 500 and 800 Hz. No systematic changes in apparent cross sections exceeding experimental

Table I. Examples of raw data.

	S_1 (counts)	S_2 (counts)	\bar{I} (nA)	\bar{J} (μ A)	F (mm)	Duty factor of gating	$\sigma(10^{-17} \text{ cm}^2)$
Ne	153928	144021	59.6	132	3.23	0.168	1.15
Ar	443096	356896	135	87	3.19	0.167	4.75
Kr	172649	57679	56.2	117	3.27	0.168	8.48
Xe	64161	14846	17.0	88.4	3.22	0.168	12.33

errors were found. It was thus concluded that the pressure modulation did not contribute significantly to the non-zero cross sections below thresholds. Problems caused by the presence of metastable ions in the ion beam will be discussed in subsection 2.8.

2.5 Form factor measurements

The form factor defined by eq. (2) can be derived from measurements of both the electron and ion current distributions along the z -axis. In the present experiment these distributions were obtained simultaneously by sliding the L-shaped shutter driven vertically at the interaction region through the two beams. The shutter was pierced by a narrow horizontal slit (0.3 mm high) so that the current density distribution could be measured. Figure 5 shows an example of these measurements. The electron beam has distributions broader than the ion beam and its intensity is roughly constant at the beam overlapping region. Then, the form factor is nearly equal to the full width at half maximum of the electron distribution in the present experiment. In other words, the form factors depend almost entirely on the electron beam profile, which varies slightly with electron energy and current. The form factor measurement was done at every point of electron energies.

The determination of the form factors with an L-shaped shutter may cause several sources of errors and difficulties. The main error comes from the geometry of the L-shaped shutter itself, which intersects the beams not at the collision center but at the position upstream before the beams collide (or downstream after they collide). As the electron beam actually diverges in this case, then the measured profiles are not strictly the same as those in the interaction region. As for the divergence of the ion beam, there is little problem for two reasons: firstly the form factor is almost independent of the ion beam profile for the present case as mentioned above, because the ion beam size is smaller than the electron beam size, and secondly the ion beam divergence is considered to be small due to the relatively long focal length of the beam.

The divergence of the electron beam causes serious problems in this experiment. In order

to evaluate this divergence, cross section measurements for Kr^{2+} were tried in the two settings of the L-shaped shutter; the shutter was placed 2 mm upstream of the collision center for measurements of one setting and 2 mm downstream for the other setting. Each set of the experiment was separated by two weeks because it was unable for the present apparatus to change the setting of the shutter without breaking the vacuum. Ratios of the apparent cross sections obtained both settings were found to differ by 13%, being approximately independent of the electron energy. This difference between the apparent cross sections was considered to be due to the divergence of the electron beam because the apparent form factors were measured at these two positions. The cross section data reported in this paper are the average of the apparent cross sections at two positions for Kr^{2+} , whereas the cross sections obtained with the 2 mm upstream setting of the shutter was corrected by multiplying a factor of 1.065 for Ne^{2+} , Ar^{2+} and Xe^{2+} . It is noted that the 13% spread of the electron beam width along 4 mm path across the collision center is found to coincide roughly to the spread due to the divergence angle subtended by the entrance slit height of the collision box to the cathode.

Further problem might arise from the introduction of the metal shutter to the beam path because secondary electrons are emitted when the beams strike the shutter. These secondary electrons cause dark current when the electron current density distribution is measured. This dark current was found to be constant at both ends of the distributions and amounted to about 3% of the peak current (see Fig. 5). Then the form factor was computed after subtracting the constant dark current. As for the ion beam distributions, no dark current was observed. An additional problem might occur because the shutter modifies electric fields within the beams. This effect was not examined in the present study, but it was expected to be negligible in the form factor measurement compared to other errors.

The computation of the form factor was carried out as follows: the multiplication of $i(z)$ $j(z)$ was made by an analog multiplier and the integrations of $i(z)$, $j(z)$ and $i(z)j(z)$ were

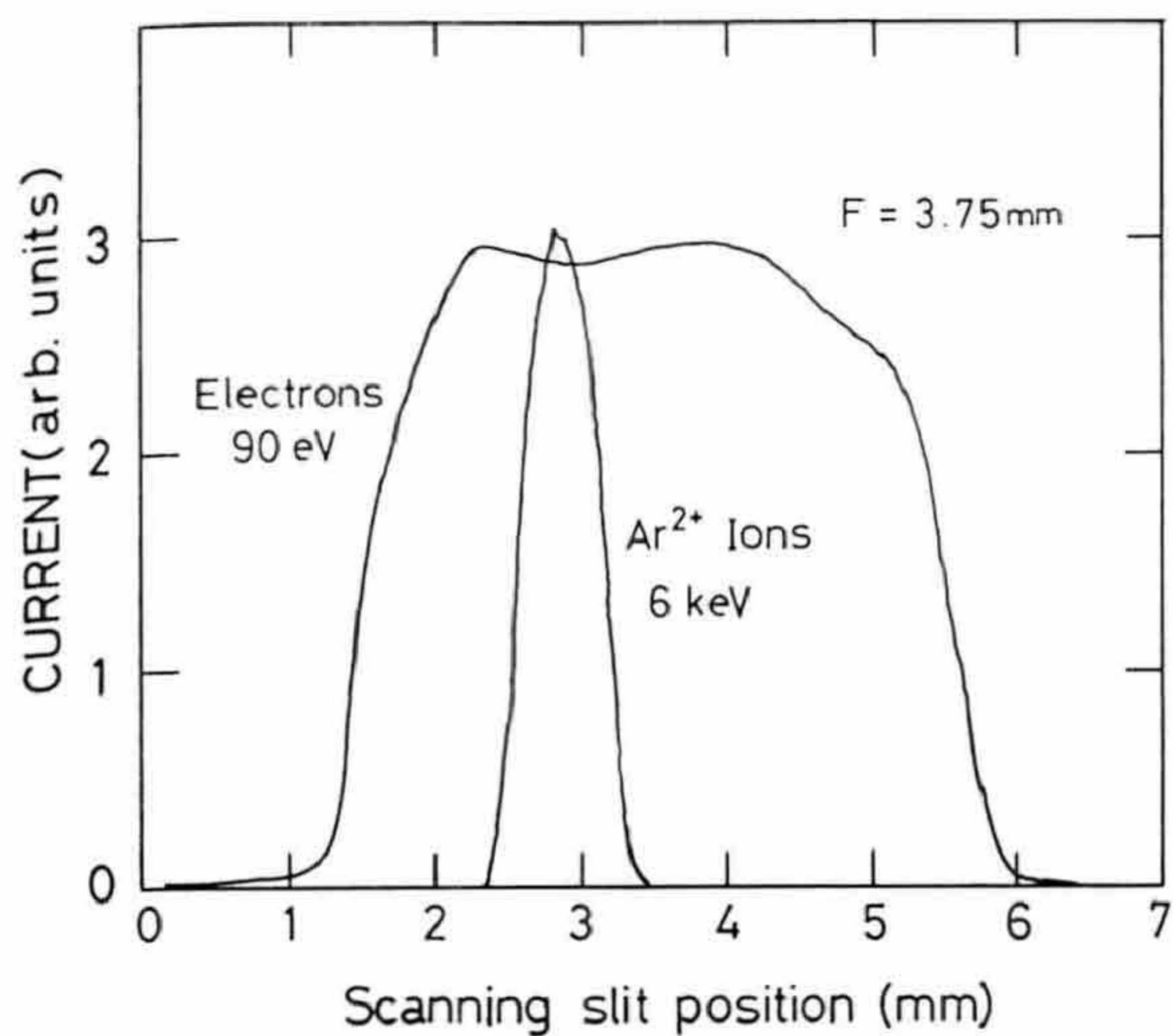


Fig. 5. Vertical distribution of electron and ion beams.

made by three voltage-to-frequency converters followed by the respective scalers under a constant scanning speed of the shutter.

2.6 Counting efficiency

As the complete transmission from the interaction region to the detector for the product ion beam is nearly fulfilled as described in subsection 2.2, the quantity D in eq. (1) reduces the counting efficiency η of the detector (MCP), which is defined as the ratio of the numbers of detected output pulses to the incident particles.

The counting efficiency of the MCP used was determined experimentally for triply charged rare gas ions of the same energy as that used for the cross section measurements. Experimental setup is illustrated in Fig. 6. The triply charged rare gas ions, obtained directly from the ion source after passing through the exit slit ($1 \times 1 \text{ mm}^2$) of the mass selector at an appropriate energy (6 keV), are diverged by a quadrupole lens (doublet) and by drifting over 40 cm. Then the ion beam is defined spatially by a rectangular aperture (8 mm in width and 10 mm in height), which is fixed to the chamber. After passing the aperture, the ion beam enters a deep Faraday cup (65 mm) with a large rectangular entrance (13 mm in width and 29 mm in height). In front of the Faraday cup are placed two electrodes, having apertures covered with coarse mesh made of fine tungsten wires, whose geometrical transpar-

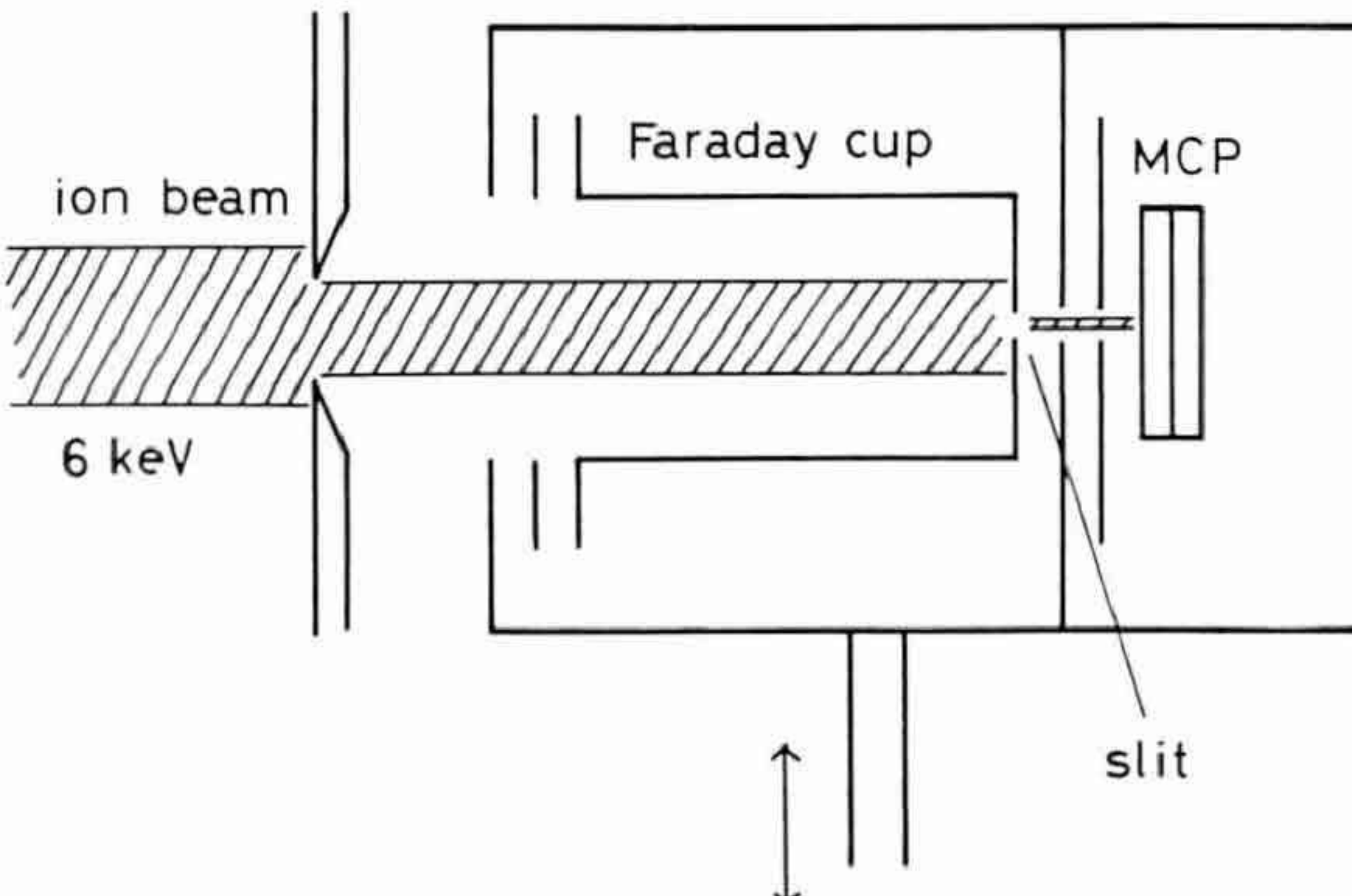


Fig. 6. Schematic diagram of the apparatus to measure the counting efficiency of the MCP.

ency is practically 100%. The first electrode is grounded and the second is for repelling secondary electrons. At the bottom of the Faraday cup is pierced a narrow horizontal slit (0.169 mm), through which a small portion (about 1.5%) of the beam flux is allowed to enter the entrance surface of the MCP. Between the bottom of the Faraday cup and the MCP, two plates with slits for beam passage are placed. This arrangement is essentially the same as those in the ion detector assembly for the cross section measurements. The Faraday cup and the MCP are mounted in a grounded shield box, which can be driven vertically through the beam. By scanning this assembly, a vertical profile of the ion beam averaged out along the horizontal axis can be obtained from the count rate of the MCP, while the total ion beam is fully caught into the Faraday cup because its entrance height is substantially larger than twice the beam height. Beam currents of triply charged ions are kept below $1 \times 10^{-13} \text{ A}$ throughout the measurement, so that the count rate of the MCP is about 3000 cps or less. It is noted that this count rate is comparable with that of the cross section measurements; the count rates of pulses from the MCP are recorded with a ratemeter as a function of slit position of the Faraday cup. The counting efficiency of the MCP is measured as follows: just after the density distribution measurement the slit is fixed at a position within the beam profile where the density distribution is relatively flat (the arrow indicates the position in Fig. 7). Then the pulses from the MCP are counted during a fixed time

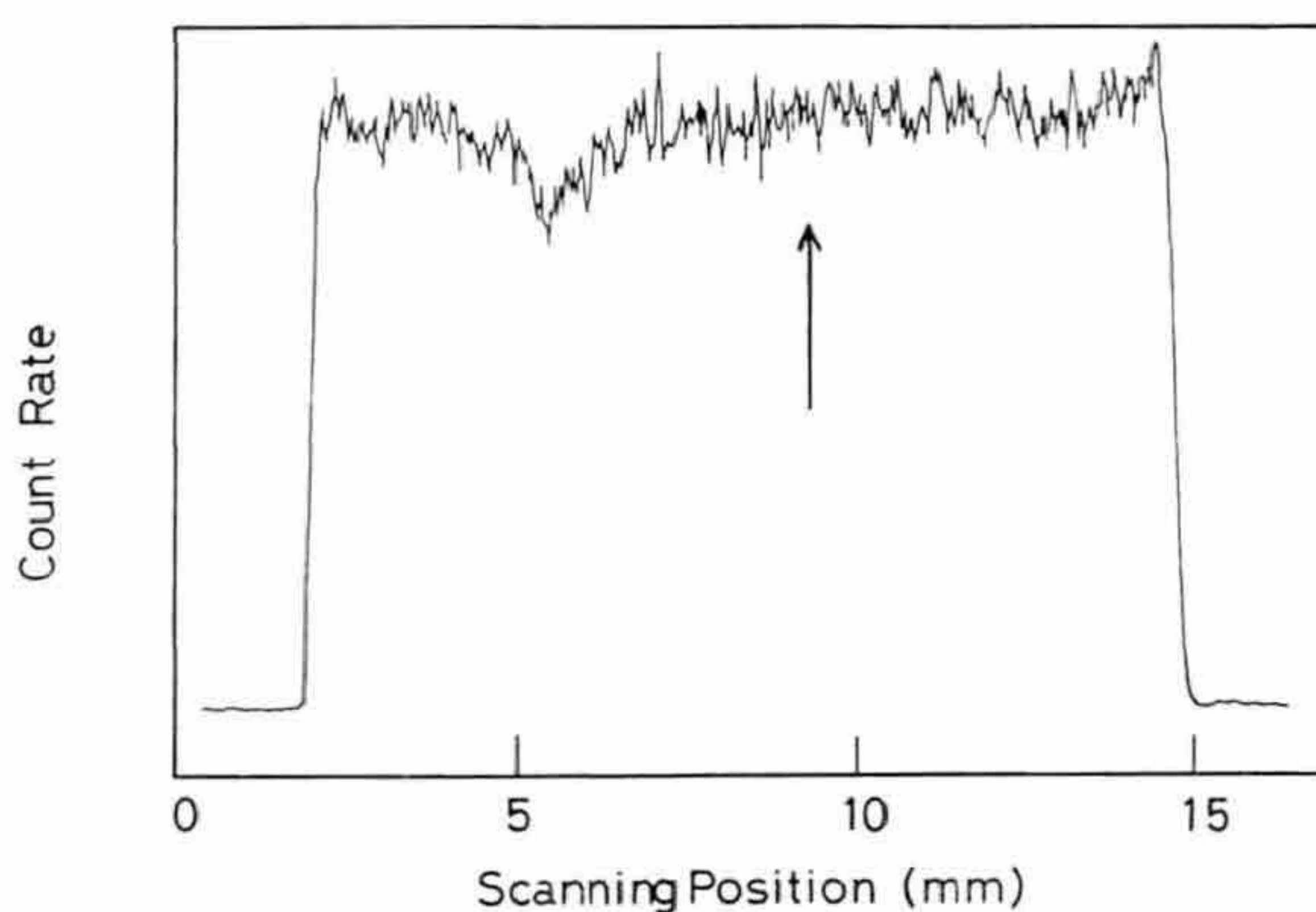


Fig. 7. Example of vertical distribution in triply charged ion beams obtained by sweeping the detector assembly across the ion beam.

(usually 100 s), while the current measured by the Faraday cup is integrated simultaneously with the voltage-to-frequency converter combined to the electrometer. The detection efficiency η is given by

$$\eta = \frac{qeS \int R dt}{dl \int I dt}, \quad (5)$$

where S is the area under beam profile curve, l the height of beam profile curve at the fixed position, $\int R dt$ the accumulated counts, $\int I dt$ the integrated current, d the width of the slit and qe the charge of ion. As the actual ion beam intensity fluctuates, the measurements are repeated several times and the results are averaged. The ion beam current measured by the Faraday cup is not strictly the total beam current since a small portion of the current passes through the slit and enters the MCP. This minor correction for the current is made as

$$I = \frac{I'}{\left(1 - \frac{d}{w}\right)}, \quad (6)$$

where d and w denote the width of the slit and the width of the measured beam profile, I and I' are the corrected and measured currents, respectively.

The operating conditions of the MCP and the relevant electric circuits are kept at the conditions set for the cross section measurements. The electrometer is calibrated against a stand-

Table II. Counting efficiencies of MCP.

Ion species	Applied voltage	
	-2.2 kV	-1.9 kV
Ne ³⁺	93 ± 8%	56 ± 5%
Ar ³⁺	92 ± 5%	56 ± 6%
Kr ³⁺	87 ± 5%	56 ± 4%
Xe ³⁺	85 ± 5%	55 ± 6%

ard current source (Keithley 261).

The counting efficiencies were checked against the potential applied to the electrode in front of the input surface of the MCP. The results are shown in Table II for two different applied voltages. Recently, similar measurements have been reported by Gao *et al.*,¹¹⁾ who examined the counting efficiencies of MCP for H⁺, He⁺ and O⁺ ions below 5 keV.

2.7 Estimation of uncertainties

All data points presented here are the average values of several independent absolute measurements. Statistical and systematic uncertainties are listed in Table III. The statistical uncertainty is ±3% at 95% confidence level for maximum cross sections for typical measurements. Systematic uncertainties associated with the measured quantities as-

Table III. Estimated uncertainties.

Items	Uncertainty (in %)
Statistical uncertainty at 95% confidence level for the maximum cross sections for typical measurements	±3
Systematic uncertainties associated with quantities assigned in eq. (1)	
Ion current I	±3
Electron current J	±4
Form factor F	±2.5
Ion velocity v_i	±0.5
Electron velocity v_e	±0.5
Transmission and counting efficiency D	±5.4
Signal count rate R for Ar ²⁺ , Kr ²⁺ , Xe ²⁺	±1
Signal count rate R for Ne ²⁺	±4
Total uncertainty (quadrature sum):	
for Ar ²⁺ , Kr ²⁺ , Xe ²⁺	±8.5
for Ne ²⁺	±9.3

signed in eq. (1) to evaluate the absolute cross section are common to four kinds of ion species except for the uncertainty in the signal count rate, which is at most $\pm 1\%$ for Ar^{2+} , Kr^{2+} and Xe^{2+} , while it is $\pm 5\%$ for Ne^{2+} . Systematic uncertainties are estimated at a good confidence level judged equivalent to 95% confidence level for statistical uncertainties.

Major origins of the systematic uncertainty are considered to be in the measurements of the electron current J and the counting efficiency D , the former coming from inaccuracy of 3% in the calibration of the microammeter and incompleteness of 2.5% in the current collection (see §2.3) and the latter from uncertainty of 5.4% in the counting efficiency of the ion detector used (see §2.6). The uncertainty in the measurement of the form factor F is believed to be suppressed to 2.5% by introducing a correction for the divergence of the electron beam (see §2.5). The uncertainty in the signal count rate R depends on the signal to noise ratio. Therefore, it varies depending on the ion species as well the electron impact energies as described in section 2.4. It is estimated to be less than 1% for Ar^{2+} , Kr^{2+} and Xe^{2+} at 100 eV impact energy, but it amounts to 4% for Ne^{2+} because of a relatively poor signal to noise ratio at the same energy. The total uncertainty, which is deduced as a quadrature sum of all uncertainties, is 8.5% for Ar^{2+} , Kr^{2+} and Xe^{2+} , and 9.3% for Ne^{2+} at the maximum cross sections.

2.8 Contribution of metastable ions

The ionization cross sections obtained in the present experiments show non-zero values even below the threshold for Ar^{2+} , Kr^{2+} and Xe^{2+} . As an example, the ionization cross sections below and near threshold for Ar^{2+} is shown in Fig. 8. In the electron configuration ns^2np^4 of the doubly charged rare-gas ions, there are three long-lived states 3P , 1D and 1S : the 3P state is the ground state and 1D and 1S are metastable. In the Ar^{2+} case, the metastable states 1D and 1S lie at 1.7 and 4.0 eV above the ground state 3P , respectively. A fraction of the metastable ion ($3p^4 \ ^1D$) in the Ar^{2+} beam extracted from the present ion

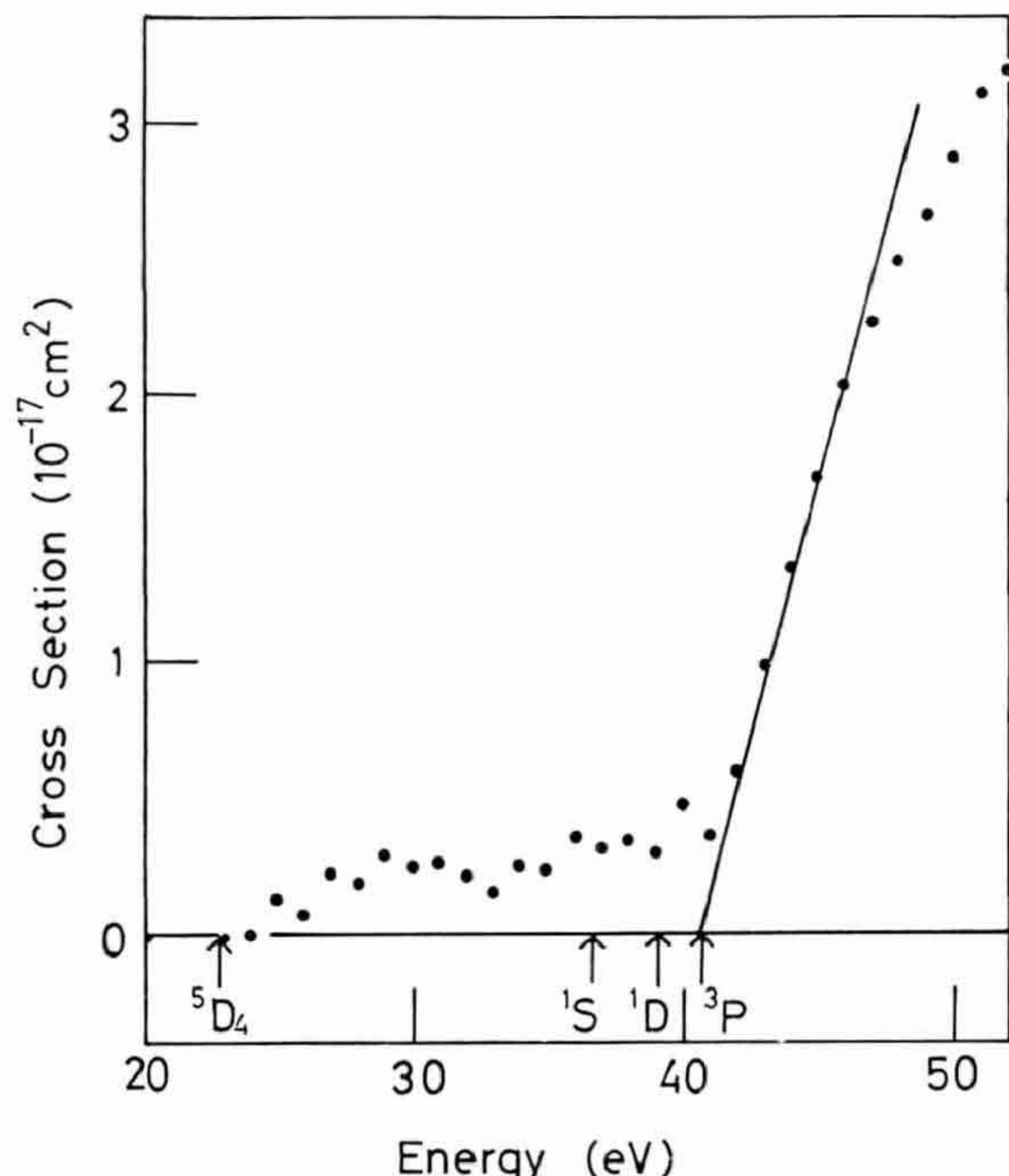


Fig. 8. Measured cross section of Ar^{2+} near and below threshold. The arrows indicate the ionization potentials for possible metastable ion states.

source was previously estimated to be nearly 30% by the optical attenuation method.¹²⁾ This estimation was made with the assumption of two beam components; i.e., the ion beam consists of the ground state ion 3P and the metastable ion 1D , where the 1S ion or other highly excited state ion were disregarded. The present cross section measurements below the threshold reveals that this assumption is not correct. In Fig. 8, the threshold energies for the ground state and two metastable states are indicated by arrows. A non-zero cross section persists down to about 22 eV impact energy. This fact suggests that not only the metastable ion 1D but highly excited metastable states $3p^4 \ ^1S$ and even $3p^3 \ ^3d \ ^5D_4$ are present in the ion beam used. Similar results are obtained for Kr^{2+} and Xe^{2+} cases. The metastable states $4d \ ^5D_4$ for Kr^{2+} and $5d' \ ^3,1G_4$ for Xe^{2+} , which lies at 17.2 and 16.4 eV higher than their ground states, respectively, are responsible for the non-zero cross sections below the ground state threshold in addition to the contribution of low-lying metastable 1D and 1S ions, which have the same electron configuration as the ground state.

Falk *et al.* obtained the ground state cross

sections for Be-like ions (B^+ and C^{2+}) by using ion beams consisting of mixtures of ions in the $2s^2 \ ^1S$ ground state and the $2s2p \ ^3P_{0,1,2}$ metastable states.¹³⁾

In the present case, it was not possible to extract the ground state cross section or the metastable fraction in the beam from the present data owing to possible existence of more than two components of metastable ions and limited accuracy below the threshold of the ground state.

§3. Results and Discussion

Measured cross sections for single ionization are tabulated in Table IV against impact energies from below the threshold to 1000 eV for Ne^{2+} , Ar^{2+} , Kr^{2+} and Xe^{2+} . Uncertainties common to all data are listed in Table III. The cross sections are plotted in Figs. 9 to 12 as a function of impact energy for Ne^{2+} through Xe^{2+} . In order to compare the experimental cross sections with those estimated by some scaling laws, the semi-empirical formula given by Lotz is used;¹⁴⁾ it is most commonly used to predict the direct ionization cross sections of atomic ions. The simplest single parameter representation proposed by Bell *et al.* is adopted:¹⁵⁾

$$\sigma(E) = 4.5 \times 10^{-14} \sum_i m_i \frac{\ln(E/I_i)}{EI_i}, \quad (7)$$

where the cross section σ for an impact electron energy E (in eV) is given in cm^2 , m_i is the number of electrons in the subshell i , and I_i is the ionization energy (in eV) for electrons in that subshell. Summation is made over the np and ns subshells to calculate the total cross sections plotted in Figs. 9–12, where n are 2, 3, 4 and 5 for Ne^{2+} , Ar^{2+} , Kr^{2+} and Xe^{2+} , respectively.

3.1 Ne^{2+}

Figure 9 shows the cross section of Ne^{2+} as a function of electron energy. The cross section increases gradually from the threshold of the 2p-electron ionization (63.45 eV by Bashkin) to reach its maximum value of $1.7 \times 10^{-17} cm^2$ at an impact energy of about 300 eV. Neither the onset of direct ionization of the 2s-electrons at 86.24 eV nor that of the 1s-electrons at 937 eV appears to have any significant effect

Table IV. Experimental cross sections for electron impact single ionization of Ne^{2+} , Ar^{2+} , Kr^{2+} and Xe^{2+} .

E (eV)	Ne^{2+}	$\sigma(10^{-17} cm^2)$ Ar^{2+}	Kr^{2+}	Xe^{2+}
17				0.0599
18				0.0095
19		-0.0416	0.233	
20		-0.0296	0.437	
21		0.0476	0.385	
22		0.0713	0.355	
23	-0.0257	0.131	0.442	
24	-0.00332	0.156	0.709	
25	0.128	0.131	0.528	
26	0.0639	0.163	0.631	
27	0.216	0.194	0.786	
28	0.185	0.214	0.719	
29	0.277	0.141	0.752	
30	0.237	0.314	0.699	
31	0.252	0.266	0.992	
32	0.207	0.100	1.78	
33	0.153	0.146	2.48	
34	0.245	0.263	4.20	
35	0.234	0.314	5.38	
36	0.343	0.452	6.32	
37	0.297	0.900	6.92	
38	0.343	1.57	7.49	
39	0.294	2.62	7.80	
40	0.470	3.22	8.25	
41	0.349	3.84	8.66	
42	0.593	4.18	8.82	
43	0.977	4.72	9.02	
44	1.35	5.14	9.36	
45	1.69	5.54	9.35	
46	2.03	6.12	9.47	
47	2.26	6.45	9.53	
48	2.49	6.74	9.62	
49	2.65		9.62	
50	2.87	7.11	9.79	
51	3.11		9.66	
52	3.20	7.44	9.80	
53	3.55		9.97	
54	3.69		10.0	
55	3.77	7.97	10.4	
56	3.86		10.5	
57	3.87	8.23	10.7	
58	4.06		10.9	
59	4.12			
60	-0.0380	4.13	8.50	11.0
61	-0.0040	4.23		
62	0.0521	4.19		11.0
63	0.0218	4.41		10.9
64	0.0872	4.53		11.2
65	0.171	4.42	8.72	11.2
66	0.0671	4.49		11.2
67	0.153			
68	0.169	4.61		11.4
69				

continued

Table IV. continued

E (eV)	Ne^{2+}	$\sigma(10^{-17} \text{ cm}^2)$	Ar^{2+}	Kr^{2+}	Xe^{2+}
70	0.298	4.71	8.91	11.5	
71				11.7	
72	0.398	4.58		12.3	
73					
74				12.4	
75	0.463	4.74	9.06	12.7	
76				12.7	
77		4.86			
78				12.8	
80	0.673	4.85	9.01	12.9	
85	0.751	4.90	8.89	12.9	
90	0.864	4.94	8.73	12.7	
95	0.971	4.85	8.69	12.4	
100	1.15	4.74	8.42	12.3	
105		4.63	8.16	11.6	
110	1.18	4.51	7.96	11.1	
112		4.49			
115		4.36	7.66	10.5	
117		4.45			
118				10.4	
120	1.29	4.39	7.44	10.3	
125		4.30	7.23	9.92	
130	1.37	4.21	7.15	9.75	
135		4.16	7.17	9.67	
140	1.42	4.14	7.20	9.46	
145		4.12	7.12		
150	1.42	4.12	7.04	9.18	
155		4.13	6.98		
160	1.47	4.08	6.93	8.81	
165			6.86		
170	1.51	4.03	6.75	8.61	
175			6.69		
180	1.55	3.98	6.62	8.46	
190	1.63	3.92	6.46	8.36	
200	1.64	3.81	6.26	7.97	
210		3.77	6.05	7.76	
220	1.65	3.68	5.88	7.60	
240	1.67	3.57	5.62	7.23	
260	1.71	3.47	5.45	6.95	
280	1.71	3.34	5.21	6.70	
300	1.17	3.22	5.01	6.31	
320		3.14		5.99	
325	1.68		4.80		
340		3.05		5.93	
350	1.67		4.56		
360		3.01		5.78	
375	1.64		4.39		
380		2.93		5.43	
400	1.64	2.84	4.26	5.38	
425	1.59	2.75	4.13	5.04	
450	1.58	2.68	3.98	4.97	
475		2.63	3.83	4.88	
500	1.58	2.51	3.70	4.75	
550	1.51	2.42	3.48	4.48	

continued

Table IV. continued

E (eV)	Ne^{2+}	$\sigma(10^{-17} \text{ cm}^2)$	Ar^{2+}	Kr^{2+}	Xe^{2+}
600	1.49	2.29		3.28	4.24
650		2.20		3.10	
700	1.40	2.09		2.94	3.89
750		1.99		2.84	
800	1.36	1.92		2.69	3.54
900	1.28	1.80		2.45	9.26
1000	1.24	1.65		2.30	3.04

on the total ionization. A metastable content in the parent ion beam is negligibly small, as indicated by zero cross section values below 63.5 eV. The result of the calculation by Lotz is also shown in Fig. 9 in order to estimate the direct ionization by a semi-empirical way. There is a large discrepancy between Lotz's calculation and the present experimental results. The Lotz formula shows a maximum at about 180 eV, and an overestimate by about 25% around this region. On the other hand, the Lotz formula underestimates the cross sections by 12% at energies higher than 800 eV.

Gregory *et al.*¹⁶⁾ have shown that Lotz's prediction gives a good agreement with the experiment over all energies between the threshold and 1500 eV for ionization of Ne^{3+} . Man *et al.*¹⁷⁾ have also shown for ionization of Ne^+ that the Lotz formula provides a very good agreement with experiment at energies

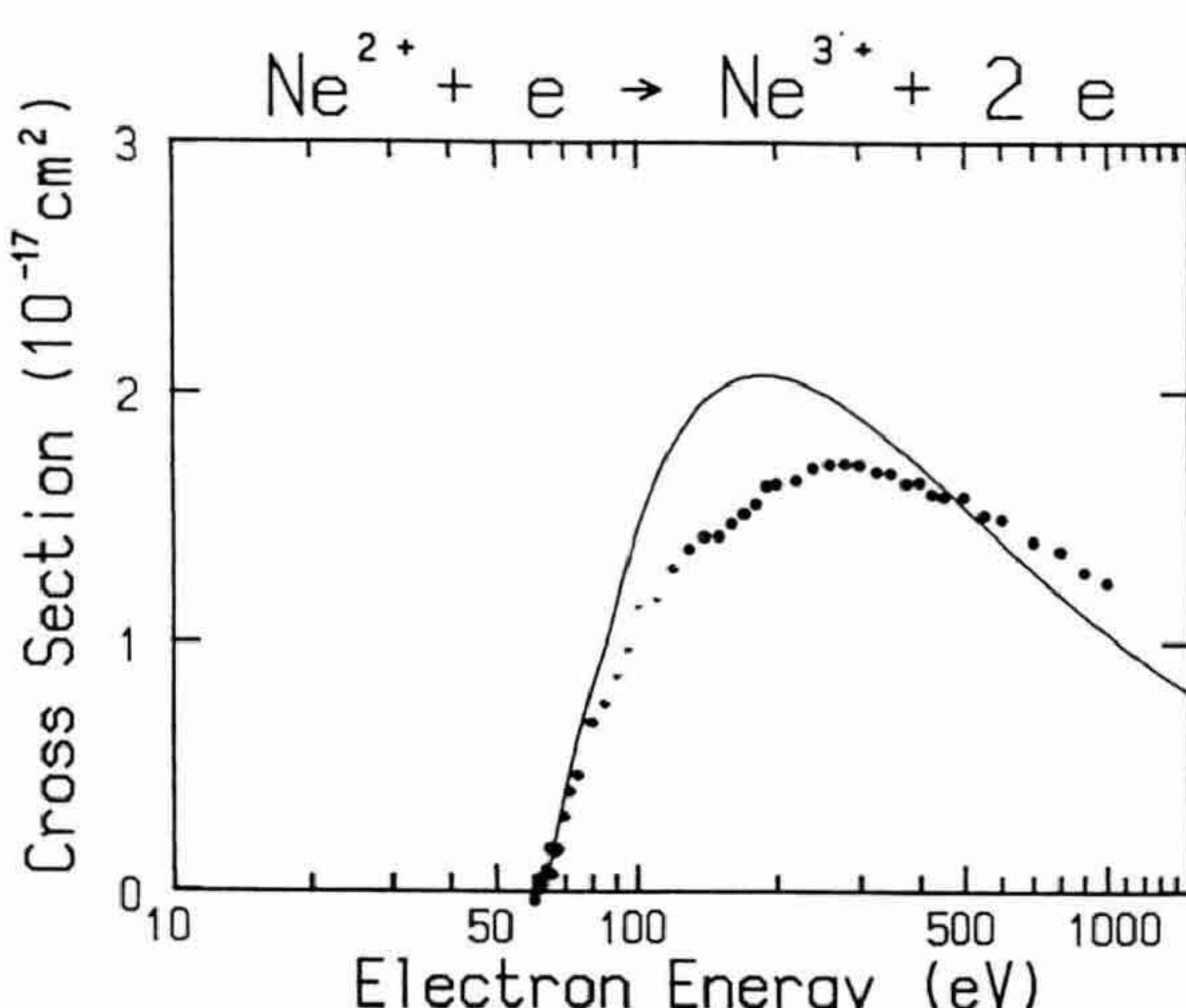


Fig. 9. Single ionization cross sections of Ne^{2+} as a function of electron energy (solid circles). The curve is based on the semiempirical formula given by Lotz.

around maximum cross sections, and it slightly underestimates the cross section at lower and higher energies. This disagreement of Lotz's prediction for Ne^{2+} is quite unexpected. No plausible explanation for the cause of this discrepancy is given at present.

3.2 Ar^{2+}

Figure 10 shows cross sections versus electron energy for ionization of Ar^{2+} . The cross sections measured by Müller *et al.*,¹⁸⁾ Mueller *et al.*,¹⁹⁾ and Diserens *et al.*²⁰⁾ are also plotted for comparison. Lotz's calculation obtained using values of 40.9 eV and 55.4 eV for the ionization energies of the 3p and 3s electrons, respectively, is also shown. Non-zero cross sections observed below the 3p-ionization threshold is due to the contribution of metastable contents in the primary ion beam, as discussed in §2.8.

The cross sections measured by previous groups show an excellent agreement with the present ones from the threshold to about 70 eV impact energy, but the results by Diserens *et al.*²⁰⁾ and Müller *et al.*¹⁸⁾ are 8 to 12% smaller than the present ones at energies higher than 70 eV. The results of Mueller *et al.*¹⁹⁾ agree well with the present ones in the whole energy region except from 100 eV to 150 eV. Even 12% discrepancy is well within

the combined absolute uncertainties of the measurements of four groups.

The experimental cross sections increase very rapidly from the threshold around 40 eV to 70 eV and far exceed the expected cross sections for direct ionization. This distinct enhancement in the cross section suggests that indirect processes, such as excitation of the 3s sub-shell electron to autoionizing states, contribute considerably to the total ionization cross section. This kind of feature is commonly observed in the ionization cross sections of ions with the electron configurations of $3s^23p^n$, while this has never been observed for ions with the electron configurations of $2s^22p^n$.^{21,22)} On the downward slope after the cross section maximum, a clear bump is observed around 160 eV in the cross section curve.

This structure has not been observed by any other groups referred to in Fig. 10. Diserens *et al.*²⁰⁾ particularly mention that they have never seen this structure in their cross section curve, which has been measured at small energy intervals and small random errors similar to those in the present study. Although Diserens *et al.* suggest that the bump structure in the present cross section curve may originate from the metastable ions in the primary beam, it is unlikely that a small content of the long-lived excited ions affects the cross section at impact energies much higher than the threshold.

We formerly attributed this structure to excitation-autoionization of the inner 2p electrons.⁷⁾ However, this interpretation must be revised, because the lowest 2p-electrons excited state ($2p^53s^23p^5$) is situated at about 260 eV, as estimated using the equivalent-core model²³⁾ and the binding energy, 287 eV, of the 2p electron in Ar^{2+} .²⁴⁾

We suggest that the structure around 160 eV is due to the contribution from a probable specific feature in the energy dependence of the 3s-ionization, which is expected by an analogy of the 3s-ionization curve in the neutral argon atom.²⁵⁾

3.3 Kr^{2+}

Results of the measured ionization cross sections for Kr^{2+} are plotted as a function of impact energy in Fig. 11 together with the ex-

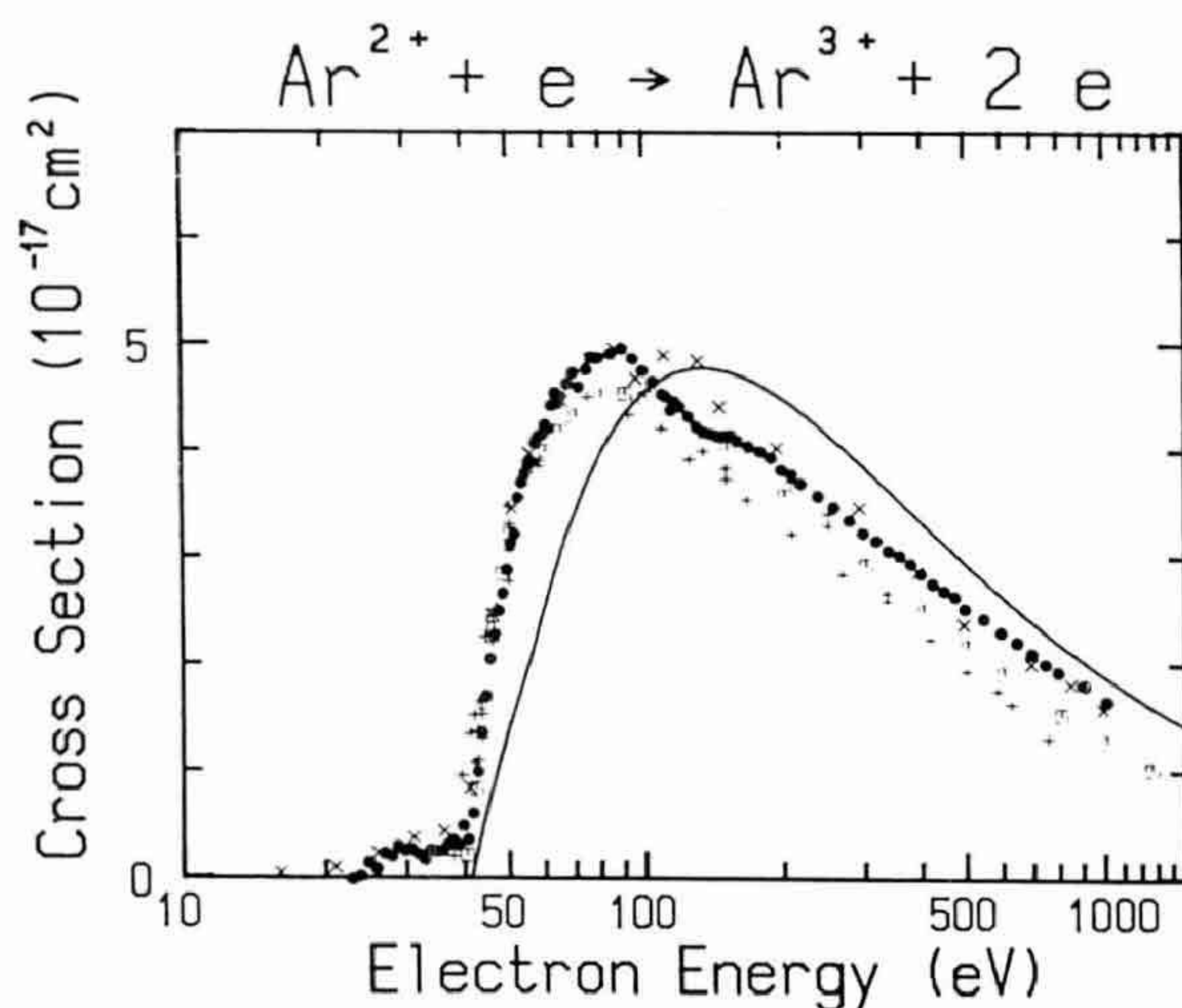


Fig. 10. Single ionization cross sections of Ar^{2+} as a function of electron energy (solid circles). Also shown are experimental results by Müller *et al.* (+), Mueller *et al.* (×), and Diserens *et al.* (□). The curve is the semiempirical calculation using the Lotz formula.

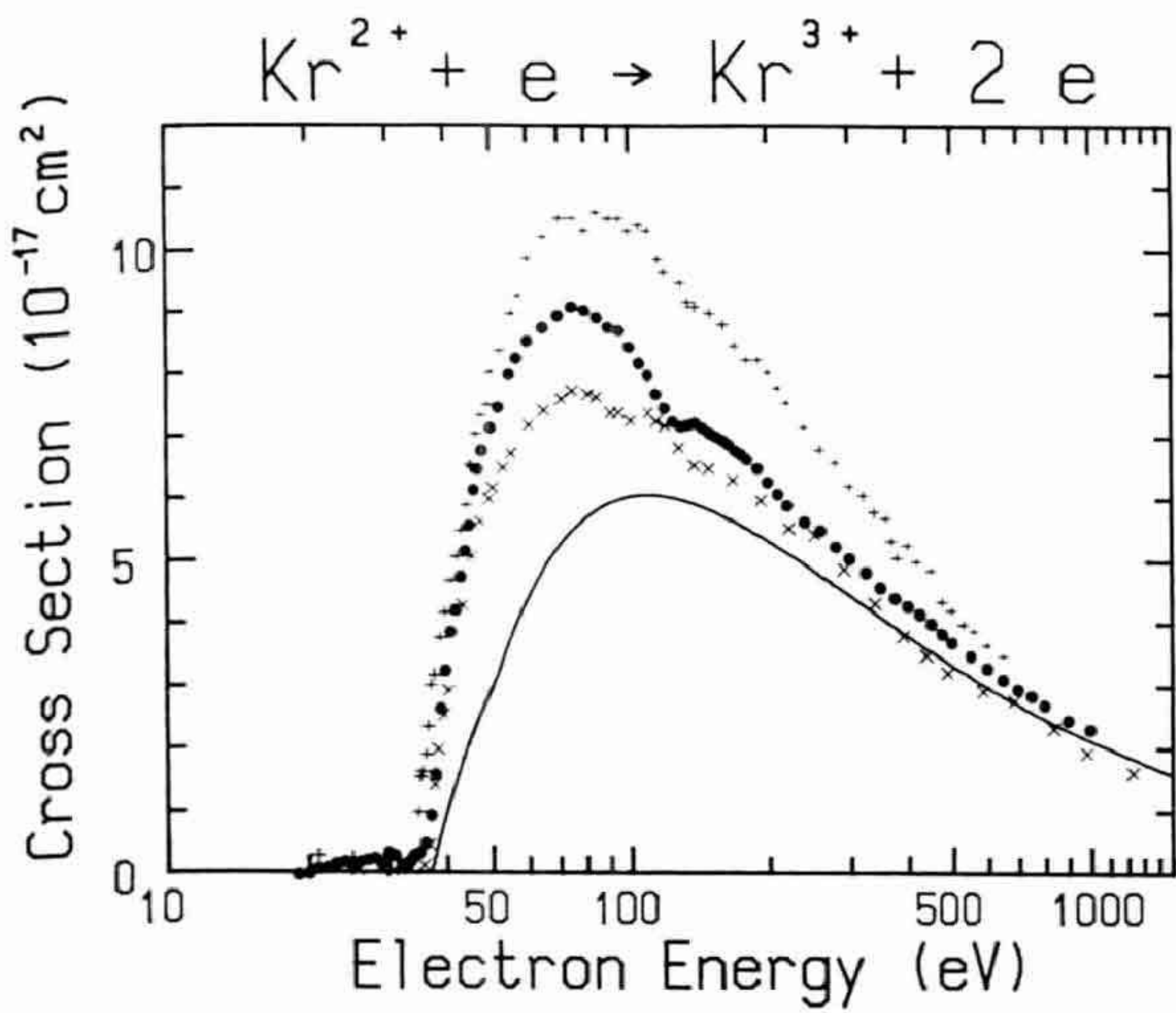


Fig. 11. Single ionization cross sections of Kr²⁺ as a function of electron energy (solid circles). Also shown are experimental results by Gregory *et al.* (×) and Tinschert *et al.* (+). The curve is the semiempirical calculation using the Lotz formula.

perimental results of Gregory *et al.*²⁶ and Tinschert *et al.*²⁷ Also shown is Lotz's calculation curve for direct single ionization of the 4p and 4s subshells with ionization energies of 36.9 eV and 51.7 eV, respectively. Non-zero cross sections are observed below the threshold region, 25 eV to 35 eV, indicating the presence of metastable ions. The cross section rises very steeply from the threshold to about 70 eV, reaching a maximum at 80 eV, and then decreases rapidly leaving a peak behind. The experimental cross sections are much greater than Lotz's calculation in the whole energy region lower than 300 eV, beyond which the cross sections approach asymptotically to the Lotz curve.

Indirect processes caused by inner-shell excitations to autoionizing levels of types



with nl=4p, 4d, and 4f may be responsible for most of the enhancement in the cross section over direct ionization, in addition to a minor contribution from the 4s subshell excitation followed by autoionization.

The experimental cross sections of Tinschert *et al.*²⁷ are 15% larger than the present results at the maximum cross section, while those of Gregory *et al.*²⁶ are 15% smaller than ours. These discrepancies might

exceed the total uncertainty of ±9% quoted by each group. A bump structure similar to that in Ar²⁺ is observed in the present cross section curve around 140 eV. We again suggest that a double-peaked shape in the energy dependence of the ionization cross section for the 4s-electrons, which is measured in the neutral krypton atom,²⁸ is responsible for this structure.

3.4 Xe²⁺

The cross section for ionization of Xe²⁺ is shown in Fig. 12 with the experimental results of Griffin *et al.*²⁹ and Achenbach *et al.*³⁰ Also shown is Lotz's calculation using 32.1 eV and 42 eV as the 5p and 5s ionization threshold energies, respectively. The present results agree very well with those of Griffin *et al.*, showing stepwise structures starting from 40 eV to reach a sharp peak at 85 eV of impact energy. On the other hand, the cross section curve of Achenbach *et al.* has a broad maximum from 40 eV to 100 eV, whose value is 50% larger than ours at 40 eV and 12% larger than ours at 80 eV that gives the cross section maximum. All experimental cross sections converge to the expected direct ionization curve at energies higher than 400 eV.

The cross sections from the threshold to about 150 eV reveal remarkable contributions from indirect ionization processes. Calcula-

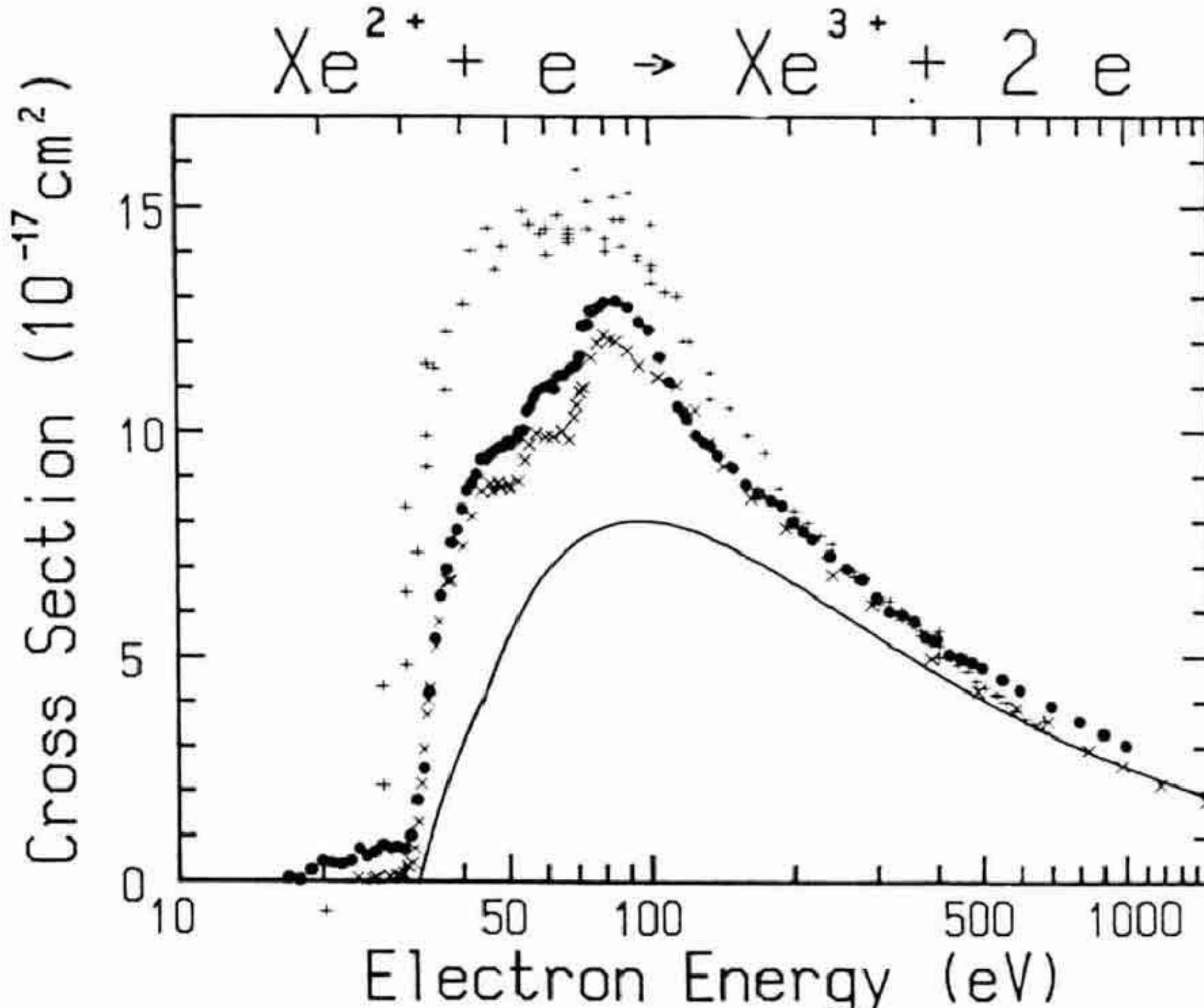


Fig. 12. Single ionization cross sections of Xe²⁺ as a function of electron energy (solid circles). Also shown are experimental results of Griffin *et al.* (×) and Achenbach *et al.* (+). The curve is the semiempirical calculation using the Lotz formula.

tions based on the distorted-wave approximation of Griffin *et al.*²⁹⁾ suggest that the increases in the cross sections at about 55 eV and over 70 to 90 eV are attributable to the inner-shell excitation to autoionizing levels of the types $\text{Xe}^{2+}(4d^{10}5s^25p^4) \rightarrow \text{Xe}^{2+}(4d^95s^25p^5)$ and $\text{Xe}^{2+}(4d^{10}5s^25p^4) \rightarrow \text{Xe}^{2+}(4d^95s^25p^4nl)$ with $nl = 4f, 5d$ and $5f$, respectively.²⁹⁾ A structure at 45 eV may be attributed to the resonant-recombination followed by double autoionization like the process



with $nl, n'l' = 5p, 4f, 5d$, etc., which suffers the transition to $\text{Xe}^{3+}(4d^{10}5s^25p^3)$ by two-electron ejection.

§4. Conclusions

We have measured the electron impact single ionization cross sections of Ne^{2+} , Ar^{2+} , Kr^{2+} and Xe^{2+} ions by means of the technique of crossed electron and ion beams. The total systematic error in the cross section is within $\pm 9\%$. In this paper we present a detailed description of the experimental apparatus and the procedures to determine the absolute cross sections. Several check points are discussed to assure the reliability and consistency of the results. Possible influence of the contents of metastable ions in the primary ion beams is discussed.

For the Ne^{2+} ion, the measured cross section curve shows a distinct disagreement with Lotz's calculation, in spite of no indication of the indirect process.

For the Ar^{2+} ion, the measured cross sections show a good agreement with those reported by other authors within the experimental uncertainties. A clear indication of indirect ionization processes is observed near the threshold energy region, which is attributed to the 3s-excitation followed by autoionization. The small bump on the downward slope after the cross section maximum is tentatively interpreted as an expected structure in the cross section curve for the 3s-ionization.

The measured cross section for Kr^{2+} are slightly larger than those reported by the Oak Ridge group but smaller than those by the Giessen group. The experimental cross sec-

tions reveal a remarkable contribution from indirect ionization processes, which are mainly attributed to the excitation of the inner 3d electrons to the autoionizing levels in addition to the 4s subshell excitation-autoionization.

The measured cross sections for Xe^{2+} show an excellent agreement with those of the Oak Ridge group. The remarkable increase in the cross sections from 55 eV to about 150 eV is attributed mainly to the excitation of the inner 4d electrons to autoionizing levels, while a possible contribution from the resonant-recombination followed by double autoionization is suggested for the increase in the cross section around 45 eV.

Acknowledgments

The authors would like to thank Professor H. Kakihana, former director of the Institute of Plasma Physics, for his encouragement. Thanks are also due to Dr. M. Kimura for his designing of the charge state analyser. We are indebted to Dr. F. Koike for his calculation of the binding energies for Xe^{2+} .

References

- 1) K. T. Dolder, M. F. A. Harrison and P. C. Thonemann: Proc. Roy. Soc. A264 (1961) 367.
- 2) Y. Itikawa, K. Takayanagi and T. Iwai: At. Data and Nucl. Data Tables 31 (1984) 215.
- 3) H. Tawara and T. Kato: At. Data and Nucl. Data Tables 36 (1987) 167.
- 4) D. C. Gregory: *Electronic and Atomic Collisions, Invited Papers of the XIV International Conference on the Physics of Electronic and Atomic Collisions*, Palo Alto, California, July 1985 (North-Holland, 1986) p. 205.
- 5) A. Müller, C. Achenbach, E. Salzborn and R. Becker: J. Phys. B 17 (1984) 1427.
- 6) S. M. Younger: in *Electron Impact Ionization*, ed. T. D. Mark and G. H. Dunn (Springer-Verlag, Wien, 1985) Chap. 1.
- 7) A. Danjo, A. Matsumoto, S. Ohtani, H. Suzuki, H. Tawara, K. Wakiya and M. Yoshino: J. Phys. Soc. Jpn. 53 (1984) 4091.
- 8) K. T. Dolder and B. Peart: Rep. Prog. Phys. 39 (1976) 697.
- 9) A. Matsumoto, S. Tsurubuchi, T. Iwai, S. Ohtani, K. Okuno and Y. Kaneko: J. Phys. Soc. Jpn. 48 (1980) 567.
- 10) M. F. A. Harrison: in *Method of Experimental Physics* Vol. 7B, ed. W. L. Fite and V. Bederson (Academic Press, New York, 1968) p. 95.
- 11) R. S. Gao, P. S. Gibner, J. H. Newman, K. A. Smith and R. F. Stebbings: Rev. Sci. Instrum. 55 (1984) 1756.

- 12) A. Matsumoto, S. Ohtani and T. Iwai: *J. Phys. B* **15** (1982) 1871.
- 13) R. A. Falk, G. Stefani, R. Camilloni, G. H. Dunn, R. A. Phaneuf, D. C. Gregory and D. H. Crandall: *Phys. Rev. A* **28** (1983) 91.
- 14) W. Lotz: *Z. Phys.* **216** (1968) 241.
- 15) K. L. Bell, H. B. Gilbody, J. G. Hughes, A. E. Kingston and F. J. Smith: *J. Phys. Chem. Ref. Data* **12** (1983) 891.
- 16) D. C. Gregory, P. F. Dittner and D. H. Crandall: *Phys. Rev. A* **27** (1983) 724.
- 17) K. F. Man, A. C. H. Smith and M. F. A. Harrison: *J. Phys. B* **20** (1987) 5865.
- 18) A. Müller, E. Salzborn, R. Frodl, R. Becker, H. Kein and H. Winter: *J. Phys. B* **13** (1980) 1877.
- 19) D. W. Mueller, T. J. Morgan, G. H. Dunn, D. C. Gregory and D. H. Crandall: *Phys. Rev. A* **31** (1985) 2905.
- 20) M. J. Diserens, A. C. H. Smith and M. F. A. Harrison: *J. Phys. B* **21** (1988) 2129.
- 21) I. Yamada, A. Danjo, T. Hirayama, A. Matsumoto, S. Ohtani, H. Suzuki, H. Tawara, T. Takayanagi, K. Wakiya and M. Yoshino: *J. Phys. Soc. Jpn.* **57** (1988) 2699.
- 22) I. Yamada, A. Danjo, T. Hirayama, A. Matsumoto, S. Ohtani, H. Suzuki, T. Takayanagi, H. Tawara, K. Wakiya and M. Yoshino: *J. Phys. Soc. Jpn.* **58** (1989) 1585.
- 23) G. C. King, M. Tronc, F. H. Read and R. C. Bradford: *J. Phys. B* **10** (1977) 2479.
- 24) W. Lotz: *J. Opt. Soc. Am.* **58** (1968) 915.
- 25) G. P. Li, T. Takayanagi, K. Wakiya and H. Suzuki: *Phys. Rev. A* **38** (1988) 1831.
- 26) D. C. Gregory: *Nucl. Instrum. Meth. in Phys. Res. B* **10/11** (1985) 87.
- 27) K. Tinschert, A. Müller, G. Hofmann, Ch. Achenbach, R. Becker and E. Salzborn: *J. Phys. B* **20** (1987) 1121.
- 28) Y. Akagi, M. Hayakawa, Y. Morikawa, T. Takayanagi, K. Wakiya and H. Suzuki: *Atomic Collision Research in Japan* **10** (1984) 24.
- 29) D. C. Griffin, C. Bottcher, M. S. Pinzola, S. M. Younger, D. C. Gregory and D. H. Crandall: *Phys. Rev. A* **29** (1984) 1729.
- 30) C. Achenbach, A. Müller, E. Salzborn and R. Becker: *J. Phys. B* **17** (1984) 1405.